

Evidence of surface p -wave superconductivity and higher-order topology in MoTe_2

Sangyun Lee,^{1,2,3,*} Myungjun Kang,^{4,*} Duk Y. Kim,⁵ Jihyun Kim,¹ Suyeon Cho,⁶ Sangmo Cheon,^{4,7,†} and Tuson Park^{1,‡}

¹*Center for Quantum Materials and Superconductivity (CQMS) and Department of Physics, Sungkyunkwan University, Suwon 16419, South Korea*

²*Los Alamos National Laboratory, Los Alamos, NM 87545, USA*

³*Department of Physics, University of Florida, Gainesville, Florida 32611-8440, USA*

⁴*Department of Physics, Hanyang University, Seoul 04763, South Korea*

⁵*Agency for Defense Development, Daejeon 34186, South Korea*

⁶*Division of Chemical Engineering and Materials Science, Ewha Womans University, Seoul, 03760, South Korea*

⁷*Research Institute for Natural Science and High Pressure, Hanyang University, Seoul 04763, South Korea*

Abstract

Exploration of nontrivial superconductivity and electronic band topology is at the core of condensed matter physics and applications to quantum information. The transition-metal dichalcogenide (TMDC) MoTe_2 has been proposed as an ideal candidate to explore the interplay between topology and superconductivity, but their studies remain limited because of the high-pressure environments required to control the topological phase transition. In this work, we demonstrate the tunable superconductivity and the resultant higher-order topology of MoTe_2 under extreme pressure. In the pressured T_d phase, Andreev reflection spectroscopy reveals two-gap features, indicating that the Weyl fermions lead to a topological s^\pm -wave multigap superconductivity. On the other hand, the high-pressure $1T'$ phase presents p -wave surface superconductivity emergent from the second-order topological bands via the bulk-to-surface proximity effect. Our analysis suggests that the topological hinge states generated from second-order topological bands evolve into zero-energy Majorana hinge states in the second-order topological superconductor. These results demonstrate the potential realization of topological superconductivity in MoTe_2 , thus opening a pathway for studying various topological natures of TMDC materials.

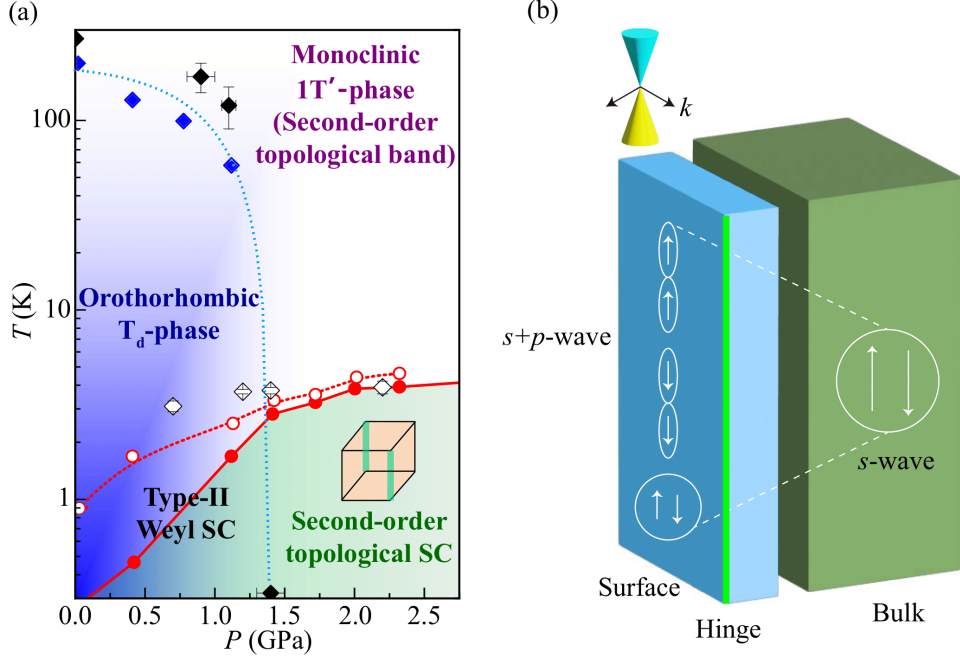


FIG. 1. **(a)** Temperature–pressure phase diagram of MoTe_2 with suggested phases. The normal $1T'$ phase hosts second-order topological insulating bands, and the SC phase becomes a second-order topological superconductor. Solid blue and black diamonds indicate the structural phase transition temperature T^* from $1T'$ to T_d phases determined from the electrical resistivity and X-ray scattering studies, respectively^{1,2}. Open and solid red circles indicate the onset temperature of the SC phase transition $T_{c, \text{onset}}$, and the zero-resistance temperature T_{zero} observed in the transport experiment, respectively¹. Open black diamonds indicate the SC transition temperature T_c obtained from our soft-point contact Andreev reflection spectroscopy, which comparably follows $T_{c, \text{onset}}$ measured in the transport measurement. The suppression of T^* coincides with a sharp increase of T_c in the T_d phase below the quantum critical point ($P_c \approx 1.4$ GPa). **(b)** Schematics for the emergence of $s + p$ -wave pairing on the surface via bulk-to-surface proximity effect between the s -wave bulk superconductivity and helical Dirac-type surface states.

I. INTRODUCTION

Transition metal dichalcogenides (TMDC) with van der Waals bonding have drawn considerable attention in condensed matter physics because they can host nontrivial topology and corresponding gapless surface states that are robust against disorder. Examples include topological insulators, crystalline insulators, Dirac/Weyl semimetals, and topological superconductors³⁻⁵. Recently, the concept of topology has been extended to materials with higher-order topology, where a d -dimensional n th-order topological material has topologically protected surface states at its $(d - n)$ -dimensional surface⁶. Although such higher-order systems have been reported in photonic systems^{7,8}, their condensed matter counterpart is still illusive^{5,9-12}.

TMDC MoTe₂ is a promising candidate for higher-order topology and topological superconductivity because of its anticipated novel topological states¹³⁻²⁰, as illustrated in Fig. 1. Theoretical studies suggested that the normal state of the bulk 1T' phase hosts a higher-order topological insulator band, where time-reversal, inversion, and translation symmetries give rise to topologically protected gapless hinge states^{9,21-24}. On the other hand, ARPES and STM experiments have reported that the normal state of the bulk T_d phase exhibits Fermi arcs, which are helical Dirac surface states arising from the Weyl fermion^{25,26}. Below the superconducting critical temperature (T_c), topological superconductivity with s^\pm -wave pairing has been proposed for the T_d phase^{27,28}. Even though the significant reduction in T_c due to disorder favors the realization of topologically nontrivial s^\pm states rather than topologically trivial s^{++} -wave pairing states in MoTe₂²⁷. The lack of further evidence has impeded their differentiation, limiting comprehensive insight into the superconductivity of type-II Weyl semimetals and their potential applications.

Here, we report evidence of the topological superconductivity of MoTe₂ and a higher-order topology using surface-sensitive soft-point-contact Andreev reflection (PCAR) spectroscopy under quasi-hydrostatic pressures. In the low-pressure T_d phase, PCAR spectra reveal two-gap features with two-step patterns, which is consistent with the suggested topological superconductivity with s^\pm pairing potential generated from type-II Weyl semimetal^{27,28}. When subject to high pressure, the resulting 1T' phase reveals evidence of the $s + p$ -wave surface superconductivity. The surface p -wave superconductivity is induced by the bulk-to-surface proximity effect between the bulk s -wave pairing and topological Dirac surface states generated from second-order topological insulator (SOTI) bands. Furthermore, a Bogoliubov-de-Gennes Hamiltonian based on the SOTI band structure reveals the potential extension of the hinge state in the SOTI phase into the Ma-

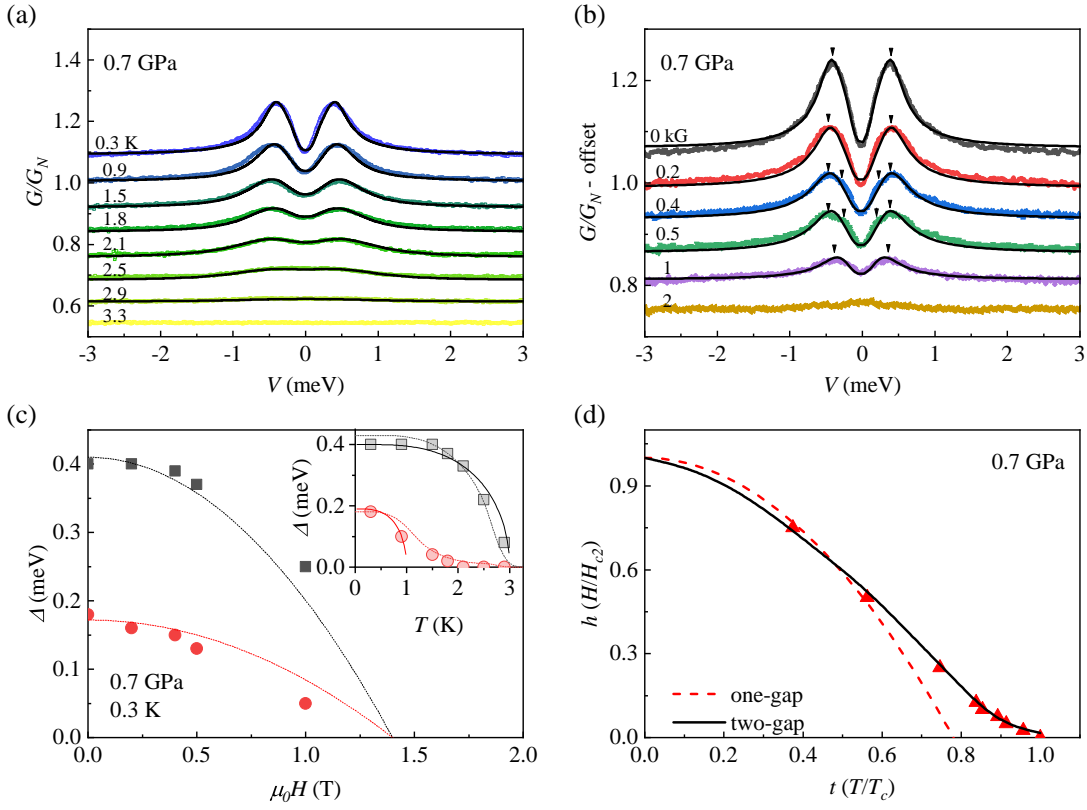


FIG. 2. **(a)** Temperature evolution of the normalized differential conductance of MoTe₂ at 0.7 GPa in the T_d phase normalized by the data at 3.3 K. The black lines are the best least-square fits of the two-gap s -wave model. **(b)** Dependence on the magnetic field of the normalized differential conductance at 0.3 K. The black arrowheads indicate the two-step features in double conductance peaks at 0.4 and 0.5 kG. In (a,b), each curve is shifted by a constant offset for clarity. **(c)** Two superconducting gaps as a function of the magnetic field. The inset shows two superconducting gaps as a function of temperature. **(d)** Reduced upper critical field ($h = H/H_{c2}$) as a function of the reduced temperature ($t = T/T_c$). Dashed red and solid black lines indicate the best fits from one-gap s -wave and two-gap s -wave BTK models, respectively.

junction hinge state in the second-order topological superconducting (SOTSC) phase through the superconducting (SC) phase transition. These results suggest that the s^\pm -wave SC state in the T_d phase evolves into a SOTSC phase of the $1T'$ phase that hosts the $s + p$ -wave surface pairings through the emergence of the inversion symmetry under high pressure.

II. RESULTS

A. Multigap superconductivity in the T_d phase under pressure

The multigap feature of the SC T_d phase under pressure is investigated via various conditions. The double conductance peaks in the differential conductance observed at 0.7 GPa below T_c , as shown Fig. 2(a), is consistent with the single s -wave SC gap. The best fittings of the Blonder-Tinkham-Klapwijk (BTK) model^{29,30}, however, indicates that it could be equally well described by the two-gap s -wave model³¹. At 0.7 GPa and 0.3 K, for instance, the best-fitting parameters for the two SC gaps (Δ) are 0.4 meV and 0.18 meV, and the gap-to- T_c ratio, $2\bar{\Delta}_i/k_B T_c$ are 3.2 and 1.4 for the large and small gaps, respectively.

The multigap nature is notably observable in the magnetic field-dependent PCAR spectra. As shown in Fig 2(b), the two-step features of each conductance peak become more profound under the magnetic fields up to 0.5 kG, as indicated by the black arrowheads. This distinctive evolution under magnetic field is consistently observed and replicated for another pressure 1.2 GPa [see Fig. S2 (b)]. Similar results have been reported for multiband superconductors such as MgB_2 and an iron-based superconductor $\text{Ba}(\text{Fe}, \text{Co})_2\text{As}_2$ ^{32,33}. The two-gap SC behavior is further demonstrated by the magnetic field dependence of the two SC gaps obtained from the two-band BTK model in Fig 2(c). The dashed lines represent the estimations of the SC gaps as a function of the magnetic field using $\Delta_i(H) = \bar{\Delta}_i(0) [1 - (H/H_{c2})^2]$, where $i = 1, 2$ for the large and small gaps, respectively³⁴, where the fitting parameters are chosen as $\bar{\Delta}_1(0) = 0.4$ meV and $\bar{\Delta}_2(0) = 0.18$ meV at 0.7 GPa and 0.3 K for consistency. These two-gap features are consistent with the muon spin relaxation (μSR) measurements, where the energy gaps are $\bar{\Delta}_1(0) = 0.43$ meV and $\bar{\Delta}_2(0) = 0.11$ meV at 1 GPa, closely aligning with our experiments of multigap superconductivity^{27,35}. Additionally, the inset illustrates the temperature dependence of the two SC gaps. While solid lines denote the temperature dependence derived from the BCS theory without interband coupling, dashed lines adequately account for a small gap with interband coupling strengths^{36,37}: $\omega_{11} = 0.39$, $\omega_{12} = \omega_{21} = 0.005$, and $\omega_{22} = 0.29$. This underscores the significance of weak interband coupling in elucidating the two-gap nature of MoTe_2 .

Supporting the multiple SC gap scenario in MoTe_2 , as depicted in Fig. 2(d), the temperature dependence of the upper critical field exhibits a discernible deviation from the conventional one-gap BCS fit (red dashed line) near T_c . The Werthamer-Helfand-Hohenberg (WHH) model³⁸ is

employed for fitting the data in Fig. 2(d), where the black line is the best fit with interband coupling strengths $\lambda_{11} = 0.38$, $\lambda_{12} = \lambda_{21} = 0.02$, and $\lambda_{22} = 0.36$. The WHH model reasonably explains the negative curvature near T_c (see details in Sec. S3). We note that disorder effects often seen in low-quality materials³⁹ are unlikely because MoTe₂ in our experiment shows a residual resistivity ratio (ρ_{300K}/ρ_{2K}) as high as 240, which is indicative of high sample quality. Furthermore, when considering previous experimental results^{27,28}, our findings in the T_d phase support the proposed topological superconductivity characterized by an s^\pm pairing potential arising from Weyl fermions as a robust and intrinsic superconductivity emerges for both ambient and pressure below the quantum critical point.

B. Surface p -wave superconductivity and higher-order nature in the $1T'$ phase at high pressure

We now examine the superconductivity and higher-order nature of the $1T'$ phase under high enough pressure that leads to a phase transition from the T_d phase. Figure 3(a) displays the temperature-dependent PCAR spectra in the pressure-induced $1T'$ phase at 2.2 GPa, where a small zero-bias conductance peak (ZBCP) is developed within the double conductance peaks below T_c . The observed ZBCP is unlikely to be due to extrinsic effects because it was not observed in the T_d phase. This indicates that it is instead associated with the pressure-induced symmetry change and the corresponding intrinsic SC properties in the $1T'$ phase.

One potential source of ZBCP is the thermal effect arising from the heating of the point contact. In such cases, the ZBCP is generally broad and exhibits limited sensitivity to weak magnetic fields due to the critical current and high normal-state resistivity^{40–42}. However, the experimental findings depicted in Fig. 3(b) do not demonstrate any characteristics indicative of the thermal regime, ruling out the contribution of heating effects to the ZBCP. Another scenario is the presence of in-gap bound states induced by magnetic impurities, which can result in symmetric or asymmetric double conductance peaks in PCAR and a ZBCP under specific conditions^{43–46}. If this were the case, the ZBCP would split into two peaks in the presence of a magnetic field, owing to the Zeeman effect. Nevertheless, as illustrated in Fig. 3(c), the ZBCP observed at 2.2 GPa remains as a single peak under the magnetic field, thus excluding the impurity scenario. Furthermore, as shown in Fig. 3(d), ZBCP is not visible at the orthorhombic T_d phase at 1.2 GPa but emerges only in the $1T'$ phase where the inversion symmetry is recovered in the high-pressure regime. These

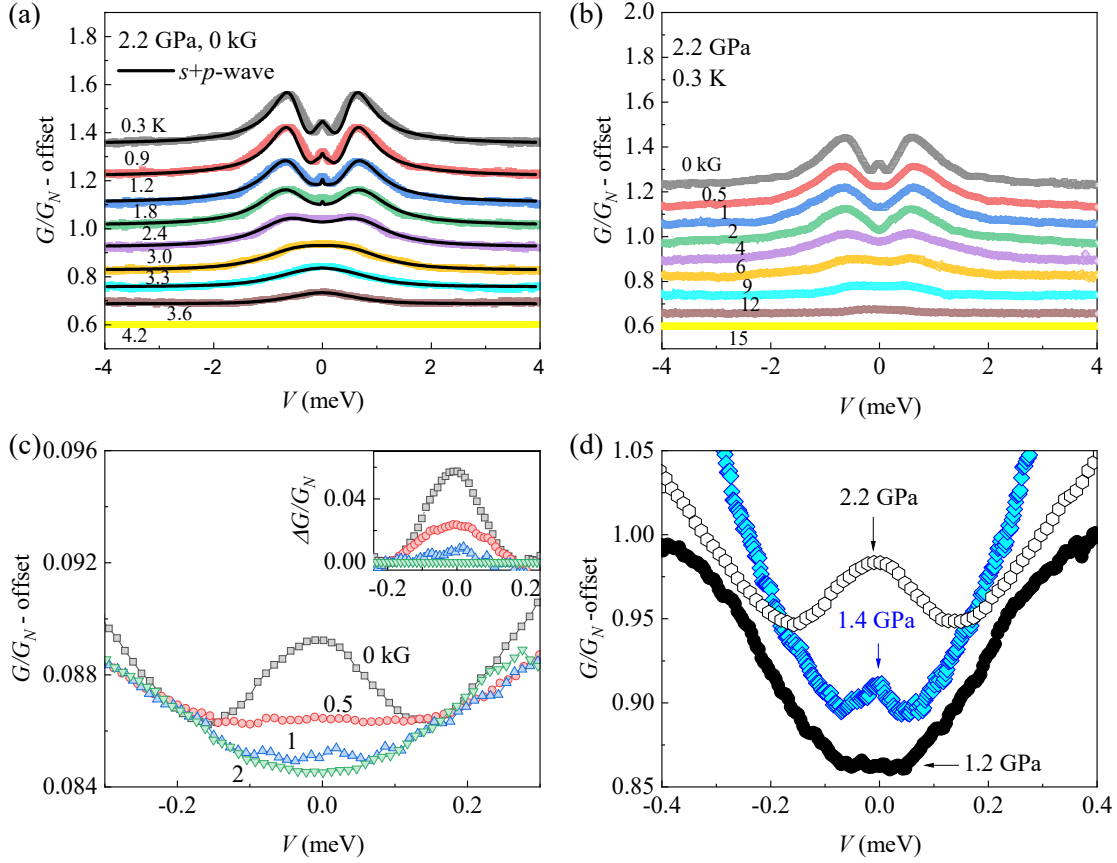


FIG. 3. Normalized differential conductance in the pressure-induced $1T'$ phase. **(a)** Temperature evolution of the normalized differential conductance at 2.2 GPa. Solid lines are the results for BTK fittings of the two-gap $s + p$ -wave model, and colored lines are measured data sets. **(b)** Normalized differential conductance under various magnetic fields at 2.2 GPa and 0.3 K. ZBCP is suppressed as the magnetic field increases. **(c)** Magnified ZBCP under various magnetic fields. For clarity, the inset shows the differential conductance after subtracting the data acquired at 2 kG for each line. The application of a magnetic field induces a progressive suppression of the ZBCP. **(d)** Evolution of the ZBCP under pressure at 0.3 K. In (a–d), each curve is shifted by a constant offset for clarity.

discoveries imply two important aspects: the ZBCP arises from the intrinsic SC properties, and it is protected by inversion symmetry.

The isotropic s -wave with a full gap cannot explain the anomalous ZBCP observed between the double conductance peaks. On the other hand, anomalous ZBCP may arise from Andreev-bound states in exotic superconductors with an anisotropic s -wave, p -wave, or d -wave superconductivi-

ties with nodes^{47,48}. However, an anisotropic s -wave scenario is improper due to the ill-fitting, as shown in Fig. S4(a). The one-gap p -wave or one-gap d -wave BTK model could lead to a ZBCP, as depicted in Figs. S3 and S4, with junction angles of $\alpha = \pi/1.35$ and $\alpha = \pi/14$, respectively. However, such fittings are obsolete due to the condition of the experimental setup being $\alpha = 0$. Taken together with the fact that d -wave superconductivity typically occurs in a tetragonal crystal structure⁴⁹, these results indicate that d -wave superconductivity is unlikely in the monoclinic $1T'$ phase of MoTe_2 . Therefore, only a variant of p -wave superconductivity remains as a candidate. Figure 3(a) shows the best fits that describe both the ZBCP and double conductance peaks of the SC gap using the $s + p$ -wave BTK model (blue lines). The fitting parameters are $\alpha = 0$ and $w = 0.5$, where w is the weighting factor of the first gap³¹.

The emergence of $s + p$ -wave pairing in the PCAR spectra can be ascribed to the bulk-to-surface proximity effect between s -wave bulk superconductivity and helical Dirac-type surface states generated from higher-order topological bands. Figure 4(a) shows the simplified band structure derived from the density functional theory (DFT) results²¹, which is composed of a hole band at the Γ point and two second-order topological insulator (SOTI) bands. The surface states generated from the SOTI bands are double copies of a topological helical surface cone with spin-momentum-locking. The form of the surface Hamiltonian is given by $H_{\text{surf}} \approx \tau_z (k_x \sigma_y - \lambda_y k_y \sigma_x)$. Due to additional Dirac mass terms in the system, the surface cones are gapless only at the hinges, resulting in topological hinge states (indicated by blue lines), a key characteristic of the SOTI⁶ (for detailed calculations, see Sec. S4.1). The most natural SC pairing mechanism is s -wave pairing for the hole band near the Γ -point. Additionally, the proximity effect induces a p -wave pairing potential at the interface between the s -wave bulk superconductivity and surface helical Dirac cones of the topological insulator⁵⁰⁻⁵². As the SOTI band structure hosts surface helical states, the p -wave pairings can be produced alongside the s -wave pairing potentials of the bulk, as shown in Fig. 1(b), which is consistent with observed $s + p$ -wave superconductivity.

C. Higher-order topological superconductivity in the $1T'$ phase

The superconductivity of the $1T'$ phase could be captured by a Bogoliubov-de-Gennes (BdG) Hamiltonian of the SC phase (See details in Methods). Since the normal state of the $1T'$ phase is a monoclinic crystal system, and the SC phase transition does not change the structure of the system, both SOTI and BdG Hamiltonians have inversion and time-reversal symmetries (i.e., PT-

symmetric). The SOTI exhibits topological hinge states protected by such PT symmetry (see more details in Fig. S5 and Sec. S4.1). With the redundant particle-hole symmetry, the BdG Hamiltonian is of the DIII class of the Altland-Zirnbauer tenfold classification, indicating the topological nature of the existing Majorana hinge state^{53,54}. As classified in Tables S1 and S3 using group theory, both s - and p -wave pairings are possible for SC pairings.

Figures 4(c) and (d) show the numerical band structure, density of states (DOS), and wavefunction distribution of Majorana hinge states for a representative p -wave pairing, where a finite tight-binding (TB) BdG Hamiltonian with finite square geometry in the xz -plane and periodic in the direction of the y -axis (C_2 rotation symmetry axis) is constructed for numerical calculations. For the analytical solution of topological Majorana hinge states, we adopt the Jackiw-Rebbi method⁵⁵. Then, the analysis indicates that the hinge of the SOTI bands expands to that of the SOTSC, as demonstrated in the schematics [Fig. 4(a,b)]³¹. As shown in Fig. 4(c), the analytical dispersion given by the Jackiw-Rebbi solution (green lines) is consistent with the numerical dispersion of the topological Majorana hinge states given by the TB method (black lines). Note that the dispersion relation of the hinge states, along with the presence of time-reversal symmetry, unequivocally establishes the helical nature of the hinge states, as shown in Fig. 4(c) and the inset in Fig. 4(d).

The localized nature of the hinges and their degeneracy is underlined by the energy eigenvalues and zero-energy wavefunction distributions of the finite TB Hamiltonian, as shown in Fig. 4(d). As expected, eight zero-energy Majorana hinge states exist due to the overlap of the two Majorana bands and PT symmetry at zero chemical potential⁵⁶. If the chemical potential is non-zero, four zero-energy Majorana states exist at different momentum (see Fig. S6). The wavefunction of such zero-energy hinge states is distributed in real space along the hinges, as shown in the inset of Fig. 4(d). Furthermore, Majorana hinge states persistently arise whenever the chemical potential is located in the gap of the SOTI bands. The band structures for zero and a representative non-zero chemical potential are plotted in Figs. S6 and S8, respectively. Note that the topological hinge states are separated from the other non-topological surface states.

Our theoretical calculations indicate that Majorana hinge states are not feasible using only s -wave pairing potentials. For the s -wave pairing case, only two possibilities arise: either the hinge states gap out, or the pairing vanishes on the surface (see Table S4). On the other hand, for p -wave pairing potentials, we find that five different pairing potentials give Majorana hinge states (see details in Figs. S6 and S7). Taken together, our theoretical and experimental results suggest

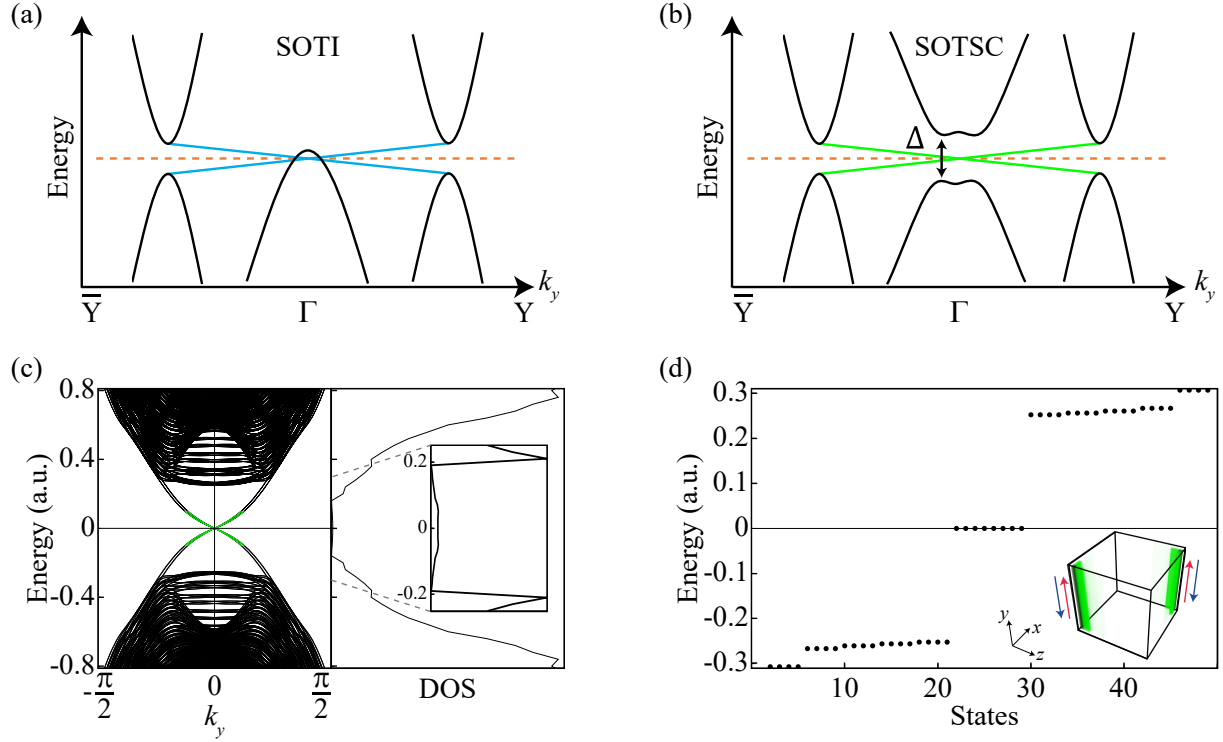


FIG. 4. **(a,b)** Schematic band diagrams for (a) the normal and (b) the $s + p$ -wave second-order topological superconducting phases. For the normal phase, the multiband is comprised of the second-order topological insulating bands and the hole band at the Γ point. The hinge states (blue lines) from the SOTI, present in (a), are transformed into Majorana hinge states (green lines) in the SOTSC. The dashed orange line indicates the position of the zero energy. **(c)** Band structures for the finite tight-binding Hamiltonian (black lines) and dispersion relation of the hinge (green line) for a nontrivial p -wave pairing $\Delta(\mathbf{k}) = \Delta_0 \sin k_y \tau_x \mu_z$. On the right, the DOS is given along the same energy axis. The inset shows the zoom-in of the DOS, and a peak can be seen at zero energy. **(d)** Energy eigenvalues at $k_y = 0$. Inset shows the probability distribution of wavefunction in real space for the eight zero-energy states, where darker color indicates higher density and the anti-propagating Kramer's pairs with time-reversal symmetry indicated by the red and blue arrows. Four helical Majorana hinges are located at one hinge, while the others are positioned on the opposite side. The parameters are the same as Fig. S6.

that symmetry-protected Majorana hinge states emerge in the SC state of the $1T'$ phase when the s -wave pairing potential exists in the bulk and surface while vanishing at the hinges. Such s -wave pairing interacts with the surface helical Dirac cones generated from the SOTI bands, leading to p -wave pairing on the surface, Majorana hinge states.

III. CONCLUSION

We investigated the superconductivity in both the T_d and $1T'$ phases of MoTe_2 through surface-sensitive soft-point contact Andreev reflection (PCAR) spectroscopy measurements under extreme conditions. In the orthorhombic T_d phase, an s -wave SC state with two-gap features was observed, which is consistent with the previously reported topologically nontrivial s^\pm -wave state²⁷. As pressure increases, MoTe_2 undergoes a phase transition from the orthorhombic T_d to the monoclinic $1T'$ phase. In the $1T'$ phase, a zero-bias conductance peak appears between the double conductance peaks in the PCAR spectra, where the extended BTK model with the $s + p$ -wave pairing consistently explains the experimental results. The emergence of the p -wave pairing in the $1T'$ phase is attributed to the bulk-to-surface proximity effect between the s -wave superconductivity of the bulk and the topological helical Dirac surface state, which is consistent with the higher-order topological nature of the normal phase. The theoretical analysis based on the BdG Hamiltonian for the second-order topological superconductor (SOTSC) phase revealed the existence of zero-energy Majorana hinge states, in the p -wave SC gap. These discoveries underpin that across the quantum critical point of MoTe_2 under pressure, the s^\pm -wave SC state in the Weyl T_d phase evolves robustly from an exotic two-gap SC state into a SOTSC phase with s - and p -wave surface pairings with the recovery of the inversion symmetry at the $1T'$ phase.

IV. METHODS

A. Experimental Methods

Under quasi-hydrostatic pressurized conditions, MoTe₂ undergoes a phase transition from the T_d to 1T' phases. To create quasi-hydrostatic pressure environments, the samples are enclosed within a Teflon tube and pressurized using a clamp-type hybrid cell filled with Daphne 7373 as the pressure-transmitting medium. This setup allows for the application of quasi-hydrostatic pressures of up to 2.7 GPa. The pressure inside the cell at low temperatures is determined by monitoring the sharp resistivity drop at the SC transition temperature of Pb and Sn^{42,57}.

Soft point-contact spectroscopy is a highly sensitive technique utilized for probing the gap structure of superconductors and the surface properties of materials²⁸. In our study, we applied this technique to investigate the gap structure of superconductivity in MoTe₂ across the phase transition from T_d to 1T'. The point contact was established using silver grains deposited on the sample surface within a quasi-hydrostatic pressure environment. After screening numerous crystals, the optimal conditions for soft point-contact spectroscopy during pressure experiments were identified. In several experiments, the contacts remained in the ballistic regime under high-pressure conditions without transitioning to the thermal regime. Temperature regulation down to 0.25 K was achieved using the ³He Heliox System (Oxford Instruments Nanotechnology).

B. Theoretical Methods

For the normal state, we consider a simplified TB model describing the SOTI bands, incorporating additional higher-order spin-orbit coupling terms to align with DFT calculations^{21,22}. The TB Hamiltonian $H(\mathbf{k})$ for the normal state of SOTI bands is given by

$$H(\mathbf{k}) = (m + \sum_{i=x,y,z} t_i \cos k_i) \tau_z + \lambda_x \sin k_x \tau_y \mu_y + \lambda_z \sin k_z \tau_x \\ + (\lambda_y \sin k_y + \lambda'_y \sin^3 k_y) \tau_z \mu_z \sigma_z + m_1 \tau_z \mu_z + m_2 \mu_x,$$

where the Pauli matrices τ_i, μ_j represent the orbital degrees of freedom and σ_k the spin degrees of freedom, respectively. λ_y, λ'_y and m_1, m_2 indicate the spin-orbital coupling terms and symmetry invariant mass terms, respectively.

By employing this SOTI TB model, we construct the Bloch BdG Hamiltonian, $H_{\text{BdG}}(\mathbf{k})$, for a potential second-order topological superconductor. This Hamiltonian considers all possible s - and

p -wave SC pairings, which is given by

$$H_{\text{BdG}}(\mathbf{k}) = \begin{pmatrix} H(\mathbf{k}) - \mu & \Delta(\mathbf{k}) \\ \Delta^\dagger(\mathbf{k}) & -H^T(-\mathbf{k}) + \mu \end{pmatrix}. \quad (1)$$

Here, $\Delta(\mathbf{k})$ is the SC paring function, and μ is the chemical potential. For SC pairings, we consider s - and p -wave pairings, which are classified using group theory and summarized in Tables S1, S2, S3 and S4. The typical s - and p -wave SC paring functions are given as $\Delta(\mathbf{k}) = \Delta_0 \tau_i \mu_j \sigma_k$ and $\Delta(\mathbf{k}) = \Delta_0 \sin k_y \tau_i \mu_j \sigma_k$, respectively.

To confirm the Majorana fermions of the hinge state, we analytically examine the surface Hamiltonian and its Jackiw-Rebbi solution. In the cylindrical geometry, we derive the surface Hamiltonian by projecting the BdG Hamiltonian over the surface localized wavevectors derived from the Dirac equation⁵⁸. The Jackiw-Rebbi method is used derive the analytical dispersion of the hinge states from the surface Hamiltonian. Further comprehensive information can be found in Sec. S4.

ACKNOWLEDGEMENTS

We acknowledge a fruitful discussion with Y. Kohama, D. Peterson, Youngkuk Kim, Kee-Su Park, and J. D. Thompson. The work at Sungkyunkwan University was supported by an NRF grant funded by the Ministry of Science and ICT (No.2021R1A2A2010925, RS-2023-00220471, 2022H1D3A01077468). The work at Hanyang University was supported by NRF of Korea through Basic Science Research Programs (Grants No. NRF-2021R1H1A1013517, NRF-2022R1A2C1011646, NRF-2022M3H3A1085772), and the POSCO Science Fellowship of POSCO TJ Park Foundation. This work was also supported by the Quantum Simulator Development Project for Materials Innovation through the NRF funded by the MSIT, South Korea (Grant No. NRF-2023M3K5A1094813). This material is based upon work supported by the US Department of Energy, Office of Science, National Quantum Information Science Research Centers, Quantum Science Center. S. L. was funded by QSC to perform data analysis and manuscript writing. A portion of this work was performed at the National High Magnetic Field Laboratory, which is supported by National Science Foundation Cooperative Agreement No. DMR-2128556* and the State of Florida.

AUTHOR CONTRIBUTIONS

S.L. performed the measurements under pressure. M.K. and S.M.C. performed the theoretical calculations. J.K. and S.Y.C. prepared the bulk samples. S.L., M.K., D.Y.K., S.M.C., and T.P. wrote the manuscript, with contributions from all authors.

* These authors contributed equally: Sangyun Lee and Myungjun Kang

† Corresponding authors:sangmocheon@hanyang.ac.kr

‡ Corresponding authors:tp8701@skku.edu

- ¹ Lee, S. et al. Origin of extremely large magnetoresistance in the candidate type-II Weyl semimetal MoTe_{2-x} . Scientific Reports **8**, 13937 (2018).
- ² Guguchia, Z. et al. Pressure Induced Topological Quantum Phase Transition in Weyl Semimetal $\text{T}_d\text{-MoTe}_2$. Journal of Physics Society of Japan **86**, 094707 (2020).
- ³ Hasan, M. & Kane, C. Topological insulators. Review of Modern Physics **82**, 3045 (2010).
- ⁴ Fu, L. Topological crystalline insulators. Physical Review Letters **106**, 106802 (2011).
- ⁵ Sato, M. & Ando, Y. Topological superconductors: a review. Reports on Progress in Physics **80**, 076501 (2017).
- ⁶ Schindler, F. et al. Higher-order topological insulators. Science Advance **4**, eaat0346 (2018).
- ⁷ Ahmed, F. et al. Deterministic Polymorphic Engineering of MoTe_2 for Photonic and Optoelectronic Applications. Advanced Functional Materials 2302051 (2023).
- ⁸ Zhu, C. et al. Nonvolatile MoTe_{2p-n} Diodes for Optoelectronic Logics. ACS Nano **13**, 7216 (2019).
- ⁹ Choi, Y.-B. et al. Evidence of higher-order topology in multilayer WTe_2 from Josephson coupling through anisotropic hinge states. Nature Material **19**, 974 (2020).
- ¹⁰ Kallin, C. & Berlinsky, J. Chiral superconductivity. Reports on Progress in Physics **79**, 054502 (2016).
- ¹¹ Fu, L. & Berg, E. Odd-Parity Topological Superconductors: Theory and Application to $\text{Cu}_x\text{Bi}_2\text{Se}_3$. Physical Review Letters **105**, 097001 (2010).
- ¹² Sato, T. et al. Fermiology of the Strongly Spin-Orbit Coupled Superconductor $\text{Sn}_{1-x}\text{In}_x\text{Te}$: Implications for Topological Superconductivity. Physical Review Letters **110**, 206804 (2013).
- ¹³ Qian, X., Liu, J., Fu, L. & Li, J. Quantum spin hall effect in two-dimensional transition metal dichalcogenides. Science **346**, 1344–1347 (2014).

- ¹⁴ Keum, D. H. et al. Bandgap opening in few-layered monoclinic MoTe₂. Nature Physics **11** (482).
- ¹⁵ Deng, K. et al. Experimental observation of topological fermi arcs in type-ii weyl semimetal mote₂. Nature Physics **12**, 1105–1110 (2016).
- ¹⁶ Zhang, K. et al. Experimental evidence for type-ii dirac semimetal in ptse₂. Physical Review B **96**, 125102 (2017).
- ¹⁷ Ma, J. et al. Experimental progress on layered topological semimetals. 2D Materials **6**, 032001 (2019).
- ¹⁸ Hsu, Y.-T., Cole, W., Zhang, R.-X. & Sau, J. Inversion-Protected Higher-Order Topological Superconductivity in Monolayer WTe₂. Physical Review Letters **125**, 097001 (2020).
- ¹⁹ Jahin, A. & Wang, Y. Higher-order topological superconductivity in monolayer WTe₂ from repulsive interactions. Physical Review B **108**, 014509 (2023).
- ²⁰ Zeng, Y. et al. Thermodynamic evidence of fractional Chern insulator in moiré MoTe₂. Nature (2023).
- ²¹ Wang, Z., Wieder, B. J., Li, J., Yan, B. & Bernevig, B. A. Higher-Order Topology, Monopole Nodal Lines, and the Origin of Large Fermi Arcs in Transition Metal Dichalcogenides XTe₂ (X= Mo, W). Physical Review Letters **123**, 186401 (2019).
- ²² Ezawa, M. Second-order topological insulators and loop-nodal semimetals in transition metal dichalcogenides XTe₂ (X= Mo, W). Scientific Reports **9**, 5286 (2019).
- ²³ Su, B. et al. Persistence of Monoclinic Crystal Structure in 3D Second-Order Topological Insulator Candidate 1T'-MoTe₂ Thin Flake Without Structural Phase Transition. Advanced Science **9**, 2101532 (2022).
- ²⁴ Benalcazar, W. A. & Cerjan, A. Chiral-symmetric higher-order topological phases of matter. Physical Review Letters **128**, 127601 (2022).
- ²⁵ Tamai, A. et al. Fermi Arcs and Their Topological Character in the Candidate Type-II Weyl Semimetal MoTe₂. Physical Review X **6**, 031021 (2016).
- ²⁶ Iaia, D. et al. Searching for topological Fermi arcs via quasiparticle interference on a type-II Weyl semimetal MoTe₂. npj Quantum Materials **3**, 28 (2018).
- ²⁷ Guguchia, Z. et al. Signatures of the topological s⁺ superconducting order parameter in the type-II Weyl semimetal T_d-MoTe₂. Nature Communications **8**, 1082 (2017).
- ²⁸ Naidyuk, Y. et al. Surface superconductivity in the Weyl semimetal MoTe₂ detected by point contact spectroscopy. 2D Materials **5**, 045014 (2018).
- ²⁹ Daghero, D. & Gonnelli, R. Probing multiband superconductivity by point-contact spectroscopy. Superconductor Science and Technology **22**, 043001 (2010).

- ³⁰ Daghero, D., Tortello, M., Ummarino, G. & Gonnelli, R. Directional point-contact andreev-reflection spectroscopy of fe-based superconductors: Fermi surface topology, gap symmetry, and electron–boson interaction. Reports on Progress in Physics **74**, 124509 (2011).
- ³¹ See more details in Supplemental Information [URL], which includes Ref.^{59–61}.
- ³² Szabó, P. et al. Evidence for two-gap superconductivity in Ba_{0.55} K_{0.45} Fe₂ As₂ from directional point-contact Andreev-reflection spectroscopy. Physical Review B **79**, 012503 (2009).
- ³³ Daghero, D., Tortello, M., Pecchio, P., Stepanov, V. & Gonnelli, R. Point-contact Andreev-reflection spectroscopy in anisotropic superconductors: the importance of directionality. Low Temperature Physics **39**, 199–210 (2013).
- ³⁴ White, R. & Tinkham, M. Magnetic-field dependence of microwave absorption and energy gap in superconducting films. Physical Review **136**, A203 (1964).
- ³⁵ Uemura, Y. J. Commonalities in phase and mode. Nature materials **8**, 253–255 (2009).
- ³⁶ Suhl, H., Matthias, B. & Walker, L. Bardeen-cooper-schrieffer theory of superconductivity in the case of overlapping bands. Physical Review Letter **3**, 552 (1959).
- ³⁷ Bogoliubov, N., Tolmachov, V. & Sirkov, D. A new method in the theory of superconductivity. Fortschritte der Physik **6**, 605–682 (1958).
- ³⁸ Gurevich, A. Enhancement of the upper critical field by nonmagnetic impurities in dirty two-gap superconductors. Physical Review B **67**, 184515 (2003).
- ³⁹ Ledvij, M. & Dovrosavljević-Grujić, L. Positive curvature in perpendicular critical field of high-temperature superconductors. Modern Physics Letters B **4**, 471 (1990).
- ⁴⁰ Wang, X.-D., Zheng, T.-F., Wang, X.-Q., Wang, Q. & Gong, W. Tunability of the andreev reflection induced by the majorana zero mode. Physica B: Condensed Matter **574**, 623 (2019).
- ⁴¹ Górski, G., Barański, J., Weymann, I. & Domański, T. Interplay between correlations and majorana mode in proximitized quantum dot. Scientific Reports **8**, 15717 (2018).
- ⁴² Eiling, A. & Schilling, J. Pressure and temperature dependence of electrical resistivity of Pb and Sn from 1-300K and 0-10 GPa-use as continuous resistive pressure monitor accurate over wide temperature range; superconductivity under pressure in Pb, Sn and In. Journal of Physics F: Metal Physics **11**, 623 (1981).
- ⁴³ Manna, S. et al. Signature of a pair of majorana zero modes in superconducting gold surface states. Proceedings of the National Academy of Sciences **117**, 8775–8782 (2020).

- ⁴⁴ Chen, J. et al. Quantum effects and phase tuning in epitaxial hexagonal and monoclinic MoTe₂ monolayers. ACS Nano **11**, 3282–3288 (2017).
- ⁴⁵ Wang, H. et al. Observation of superconductivity induced by a point contact on 3D Dirac semimetal Cd₃As₂ crystals. Nature Materials **15**, 38–42 (2016).
- ⁴⁶ Aggarwal, L. et al. Unconventional superconductivity at mesoscopic point contacts on the 3D Dirac semimetal Cd₃As₂. Nature Materials **15**, 32–37 (2016).
- ⁴⁷ Kashiwaya, S. & Tanaka, Y. Tunnelling effects on surface bound states in unconventional superconductors. Reports on Progress in Physics **63**, 1641 (2000).
- ⁴⁸ Deutscher, G. Andreev–Saint-James reflections: A probe of cuprate superconductors. Reviews of modern physics **77**, 109 (2005).
- ⁴⁹ Wenger, F. & Östlund, S. d-wave pairing in tetragonal superconductors. Physical Review B **47**, 5977 (1993).
- ⁵⁰ Stanescu, T. D., Sau, J. D., Lutchyn, R. M. & Sarma, S. D. Proximity effect at the superconductor–topological insulator interface. Physical Review B **81**, 241310 (2010).
- ⁵¹ Fu, L. & Kane, C. L. Superconducting proximity effect and Majorana fermions at the surface of a topological insulator. Physical Review Letters **100**, 096407 (2008).
- ⁵² Tkachov, G. Probing the magnetoelectric effect in noncentrosymmetric superconductors by equal-spin andreev tunneling. Journal of Physics: Condensed Matter **31**, 055301 (2018).
- ⁵³ Schnyder, A. P., Ryu, S., Furusaki, A. & Ludwig, A. W. Classification of topological insulators and superconductors in three spatial dimensions. Physical Review B **78**, 195125 (2008).
- ⁵⁴ Khalaf, E. Higher-order topological insulators and superconductors protected by inversion symmetry. Physical Review B **97**, 205136 (2018).
- ⁵⁵ Jackiw, R. & Rebbi, C. Solitons with fermion number 1/2. Physical Review D **13**, 3398 (1976).
- ⁵⁶ Yan, Z. Higher-order topological odd-parity superconductors. Physical Review Letters **123**, 177001 (2019).
- ⁵⁷ Walker, I. Nonmagnetic piston–cylinder pressure cell for use at 35 kbar and above. Review of Scientific Instruments **70**, 3402 (1999).
- ⁵⁸ Schindler, F. Dirac equation perspective on higher-order topological insulators. Journal of Applied Physics **128** (2020).
- ⁵⁹ Werthamer, N., Helfand, E. & Hohenberg, P. Temperature and Purity Dependence of the Superconducting Critical Field, H_{c2}. III. Electron Spin and Spin-Orbit Effects. Physical Review B **147**, 295 (1966).

- ⁶⁰ Bhoi, D. et al. Interplay of charge density wave and multiband superconductivity in $2\text{H-Pd}_x\text{TaSe}_2$. Scientific Reports **6**, 24068 (2016).
- ⁶¹ Cheon, S., Lee, K. H., Chung, S. B. & Yang, B.-J. Emergence of topological superconductivity in doped topological Dirac semimetals under symmetry-lowering lattice distortions. Scientific Reports **11**, 18539 (2021).